$CoFe_2O_4$ on Mica Substrate as Flexible Ethanol Gas Sensor in Self-Heating Mode

Jong Hun Kim , Yeong Uk Choi , Jong Hoon Jung * , Jae-Hun Kim *

Posted Date: 21 February 2024

doi: 10.20944/preprints202402.1218.v1

Keywords: CoFe2O4; Mica; Gas sensor; Ethanol; Sensing mechanism

Article

$CoFe_2O_4$ on Mica Substrate as Flexible Ethanol Gas Sensor in Self-Heating Mode

Jong Hun Kim [1], Yeong Uk Choi [1], Jong Hoon Jung [1,*] and Jae-Hun Kim [2,*]

[1] Department of Physics, Inha University, Incheon 22212, Republic of Korea; jh_kim@inha.ac.kr (J.H.K.); aowlr8945@gmail.com (Y.U.C.)
[2] Department of Materials Science and Engineering, Inha University, Incheon 22212, Republic of Korea
* Correspondence: jhjung@inha.ac.kr (J.H.J.); jaehun@inha.ac.kr (J.-H.K.)

Abstract: In this study, a novel flexible ethanol gas sensor was created by the deposition of $CoFe_2O_4$ (CFO) thin film was on a thin mica substrate using pulsed laser deposition. Transition electron microscopy (TEM) investigations clearly demonstrated the successful growth of CFO on the mica, where a well-defined interface was observed. Ethanol gas-sensing studies showed optimal performance at 200 °C, with the highest response, 19.2, to 100 ppm ethanol. Operating the sensor in self-heating mode under 7 V applied voltage, which was corresponds to a temperature of approximately 200 °C, produced a maximal response to ethanol of 19.2. This aligned with the highest responses observed during testing at 200 °C, confirming the sensor's accuracy and sensitivity to ethanol under self-heating conditions. In addition, the sensor exhibited good selectivity to ethanol and excellent flexibility; maintaining its high performance after bending and tilting up to 5000 times. As this is the first report on flexible self-heated CFO gas sensors, we believe that this research holds great promise for the future development of high-quality sensors based on this approach.

Keywords: $CoFe_2O_4$; mica; gas sensor; ethanol; sensing mechanism

1. Introduction

Ethanol is commonly used as a raw material, solvent, and thinner in chemical engineering, agriculture, the pharmaceutical industry, food manufacturing, and clinical and medical applications [1–3]. However, it is flammable with an explosion range of 3.3–19% [4]. In addition, excessive inhalation, consumption or similar exposure to ethanol causes drowsiness, irritation of the eyes, liver damage, breathing difficulties, headache, vertigo, nausea, fatigue, and even anesthesia and damage to the nervous system [5–7]. Ethanol consumption by drivers is a major contributor to automotive accidents, with impairment and crash risk rising significantly at blood alcohol concentrations over 425 ppm [8]. Detecting ethanol in a driver's exhaled breath can help identify intoxication and reduce or prevent alcohol-related accidents [9]. Ethanol is also considered a biomarker and measurement of skin ethanol gas can be used to detect human volatile organic chemicals in blood [10]. Ethanol sensing thus has important applications for health monitoring and public safety by enabling the non-invasive determination of blood alcohol content and impaired driving. There is a clear need for robust ethanol detection from both an accident prevention and a diagnostic screening perspective.

Resistive gas sensors are among the most prevalent materials for detecting ethanol and other gases because of their high sensitivity, high stability, rapid response time, and low cost [11,12]. These sensors are primarily based on semiconducting metal oxides [13]. However, they exhibit high operating temperatures (high power consumption), poor selectivity, and high-humidity interfaces [14]. Accordingly, it is necessary to further explore the sensing properties of the less-studied metal oxides to identify new opportunities in the field of resistive gas sensors.

Cobalt ferrite ($CoFe_2O_4$) has a spinel crystal structure [15] and good magnetic properties (hard ferrite), mechanical hardness, and chemical stability [16]. Furthermore, it is semiconducting in nature and is therefore used in gas-sensing applications [17,18]. For example, Wei et al. [19], reported synthesis of CFO NPs for ethanol sensing, where a response of 110 to 100 ppm ethanol was recorded at 200 °C. In another study, CFO NRs were prepared for acetone sensing and at 350 °C, and a response

 doi:10.20944/preprints202402.1218.v1

of 57% to 500 ppm acetone was reported [20]. Rathore et al. reported a response of 45% to 200 ppm ethanol at 250 °C [21]. Xiangfeng et al. [22], reported a response of 4 to 10 ppm ethanol at 150 °C. As shown in the examples above, CFO sensors generally operate at relatively high temperatures, which can limit their application in remote areas. Thus, it is necessary to reduce power consumption using different strategies. Operation of the sensor in self-heating mode is a feasible strategy to reduce power consumption through the application of external voltages to the sensor electrodes, where heat is generated via the Joule heating effect [23,24]. Furthermore, for new applications, rigid sensors are not appropriate for universal application, and sometimes flexibility is required. Flexible substrates such as paper, plastic, and polymers are widely used to realize flexible gas sensors owing to their high flexibility, low cost, and high availability. However, they have some limitations: their thermal stability is not generally high and they can exhibit high thermal expansion, which makes them inappropriate for materials with low thermal expansion coefficients [25,26]. Therefore, in this study, mica sheets were used as flexible substrates because of their high thermal stability, good mechanical flexibility, and low cost [27,28].

Motivated to address the lack of flexible and self-heating CFO gas sensors, we developed a highly sensitive ethanol sensor with good flexibility and low-power self-heating mode operation. Initially, CFO thin films were directly deposited onto a mica substrate using pulsed laser deposition (PLD), which offers the advantages of adaptability, good control over the growth rate, and excellent stoichiometric transfer [29]. Subsequently, the gas-sensing properties were measured in ethanol. Under external heating, the sensor performed optimally at 200 °C. However, to reduce power consumption, the sensor was operated in self-heating mode under different applied voltages, showing an enhanced response to ethanol gas at 7 V. Furthermore, after bending and tilting for up to 10 000 cycles, the sensor successfully detected ethanol, confirming its high flexibility.

2. Experimental Section

2.1. Sample Preparation

Transparent and flexible fluorophlogopite mica $KMg_3(AlSi_3O_{10})F_2$ (referred to hereafter as mica) was utilized as the sample substrate. The mica slab was pre-treated with deionized water and mechanically exfoliated to ensure an atomically smooth surface along the (001) direction. Subsequently, a CFO thin film was deposited on the mica surface using PLD, where a Q-switched 4ω Nd:YAG laser (λ = 266 nm, 10 Hz) was focused on the stoichiometric CFO ceramic target, located 5 cm away from the sample surface, with a laser fluence of 0.82 J/cm^2. During the deposition, the temperature of the mica substrate was 650 °C and the oxygen partial pressure was 0.04 mTorr. The deposited CFO film firmly adhered to the mica without failure. Based on our previous study [30], the deposition rate was fixed at 0.018 nm/pulse, and a layer-by-layer growth method was used to apply the CFO thin film.

2.2. Characterizations

The crystalline structures of the films were characterized by high resolution X-ray diffraction (XRD; D8 Discover, Bruker) using Cu-$K\alpha_1$ radiation (λ = 0.15406 nm). The vertical structure of the CFO/mica was investigated by aberration-corrected scanning transmission electron microscopy (AC-STEM; JEM-ARM200F, JEOL) at a beam energy of 200 kV. For the AC-STEM measurements, cross-sections of the films were prepared using a focused ion beam.

2.3. Gas Sensing Tests

To fabricate the gas sensors, a double-layer interdigitated electrode composed of Ti (50 nm) and Pt (200 nm) was sputtered onto the specimens over a SiO_2 substrate. Gas-sensing measurements were performed by electrically connecting the sensors to a Keithley 2400 source meter, and the data were recorded on a computer. During the measurements, the gas sensors were placed in the gas chamber of a horizontal tube furnace. The target gas concentration was set by controlling the mixing ratio of the dry-air-balanced target gas and dry air using mass-flow controllers. The resistance of the gas

 doi:10.20944/preprints202402.1218.v1

sensor was recorded in the presence of air (R_a) and target gas (R_g), and the gas response was calculated as $R=R_a/R_g$.

3. Results and Discussion

3.1. Characterization Studies

Figure 1a shows the XRD pattern of CFO on mica, where peaks related to CFO (red squares) and mica (blue spheres) are observed. The high-intensity peaks are associated with Bragg reflections produced by various pairs of mica layers, indicating the maintenance of a high-quality layered mica structure during the PLD deposition. This is attributed to the high melting temperature of mica (~1200 ˚C) [31]. However, the presence of only CFO$_{(hhh)}$ peaks implies the growth of CFO layers on mica, favoring the crystallographic relationship of CFO $_{[111]}$//mica $_{[001]}$. As the cubic structure of CFO (a =8.394 Å) is different from the monoclinic structure of mica (a = 5.187 Å, b = 9.015 Å, c = 10.131 Å, and β～ 100°), conventional epitaxial growth using strong chemical interaction is restricted at this exotic hetero-interface. In contrast, van der Waals (vdW) epitaxial (or quasi-vdW epitaxial) growth utilizes weak but long-range vdW interactions rather than the strong chemical bonds observed in conventional epitaxial growth, enabling a larger tolerance of lattice mismatches [32]. Although mica often forms a pseudohexagonal lattice with its matching condition to accommodate the large lattice mismatch, it can be advantageous for forming vdW epitaxy in heterogeneous systems [33,34].

To further investigate the structure of the CFO/mica, a cross-sectional TEM study was performed. The high-resolution TEM image (Figure 1b,c) shows that a CFO film with a thickness of approximately 240 nm was deposited on the mica substrate. There is a clear interface between the CFO and mica, where a highly crystalline CFO film is well synthesized on a flat mica substrate. Additionally, we used fast Fourier transform (FFT) images in the insets, each taken individually from the CFO film and mica substrate near the interface. The zone axes of CFO and mica were calculated as $[1\bar{1}0]$ and [010], respectively. The clear dots in the FFT images verify not only the fact that CFO $_{[111]}$ is synthesized on the mica [001] along the vertical direction, but also that CFO $_{[1\bar{1}0]}$ is laterally formed along the mica $_{[010]}$ surface, maintaining the epitaxial relation. Moreover, the well-indexed lattice points without any ring patterns or signal blurring in the FFT were consistent with the XRD results, implying the rare presence of defects or granular structures. Based on the XRD and TEM results, a schematic of the growth structure of CFO on the mica substrate was generated, as shown in Figure 1d.

 doi:10.20944/preprints202402.1218.v1

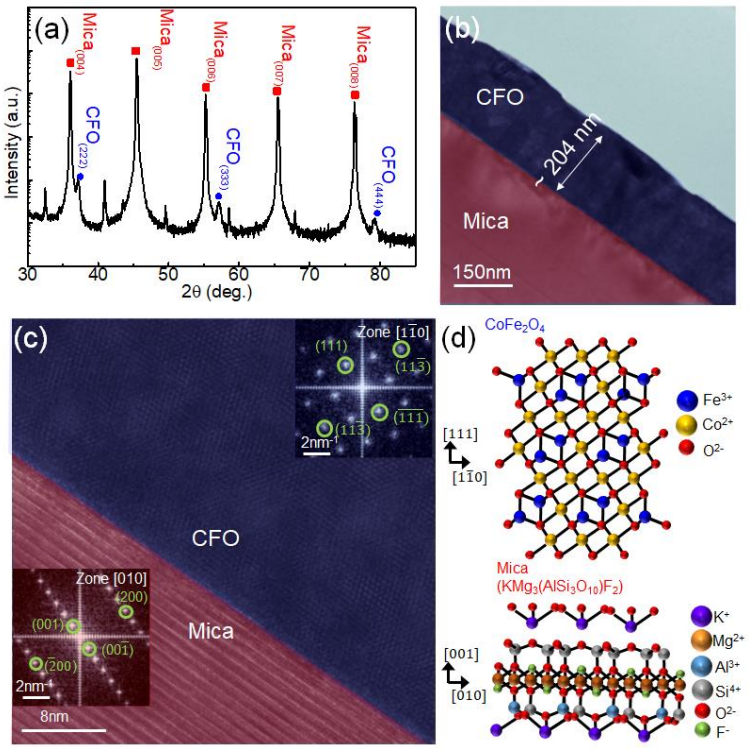

Figure 1. (**a**) XRD pattern of CFO film on a mica substrate. (**b**) Cross-sectional TEM image of CFO/mica. (**c**) False-color TEM image magnified from the interface of Figure 1b. Insets in each region shows the corresponding FFT patterns, revealing the high-quality heteroepitaxy between CFO and mica. (**d**) Schematic illustration of CFO crystal structure formed on a mica substrate via vdW epitaxy.

3.2. Gas Sensing Studies

Initially, the fabricated gas sensor was exposed to 100 ppm ethanol at various temperatures from room temperature to 350 °C to find its optimal sensing temperature (Figure 2a). The resistance decreased upon exposure to ethanol, reflecting its n-type nature. The response was calculated by increasing the temperature, which was raised to 200 °C, where a response of 19.2 was recorded (Figure 2b). A further increase in the sensing temperature led to a decrease in the response owing to the dominance of the desorption of ethanol relative to adsorption. With increasing temperature, the resistance continuously decreased owing to the jumping of electrons from the valence band to the conduction band of the sensor.

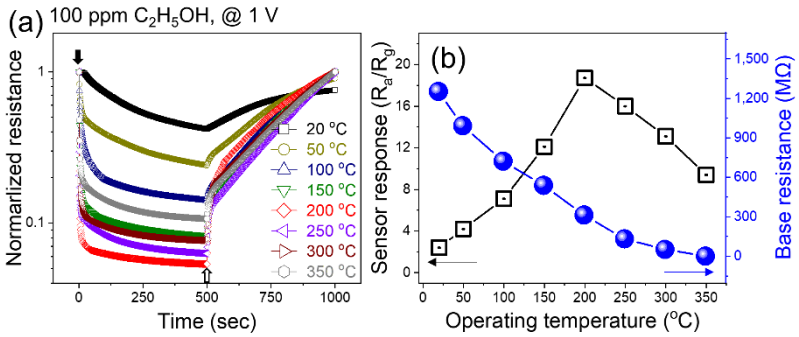

Figure 2. (**a**) Dynamic normalized resistance curves of the sensor to 100 ppm C_2H_5OH at various temperatures. (**b**) Corresponding response and base resistance of the sensor versus temperature.

Next, the sensor was exposed to 100 ppm ethanol gas under various applied voltages (Figure 3a). The response increased with increasing applied voltage up to a maximum of 7 V, and then decreased (Figure 3b). Under 7 V applied voltage the sensing temperature was approximately 200 °C,

 doi:10.20944/preprints202402.1218.v1

which was in accordance with the external heating experiments (Figure 2b). Accordingly, decrease in the response at higher voltages was due to generation of a high amount of heat, which increased the sensor temperature beyond 200 °C, where the desorption rate was higher than the adsorption rate. Upon the application of voltage, heat was generated inside the sensor due to a loss of kinetic energy of electrons when incident with other electrons or ions in their pathways. In addition, increasing the applied voltage causes more electrons to jump into the conduction band, resulting in a decrease in resistance.

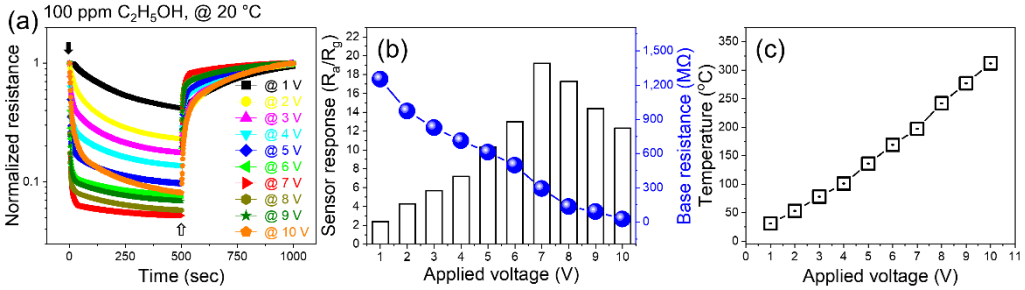

Figure 3. (**a**) Dynamic normalized resistance curves of the sensor to 100 ppm C_2H_5OH at various applied voltages. (**b**) Corresponding response and base resistance versus applied voltage. (**c**) Generated temperature versus applied voltage.

For practical applications, the sensor should display good selectivity for ethanol gas. Therefore, to study the selectivity of the sensor, it was exposed to various gases. Figure 4a shows the dynamic resistance curves of the sensor to 100 ppm of various gases at an applied voltage of 7 V, and Figure 4b shows the corresponding selectivity graph. The responses to 100 ppm ethanol, methane (CH_4), ammonia (NH_3), carbon monoxide (CO), and acetone (C_3H_6O) gases were 19.2, 5.4, 2.5, 3.2 and 8.1, respectively. Thus, the sensor exhibited good selectivity for ethanol gas. Figure 4c shows the repeatability of the sensor's performance during five sequential cycles with 100 ppm ethanol under an applied voltage of 7 V. The responses during first, second, third, fourth and fifth cycles were 19.2, 19.3, 19.1, 19, and 19.3, respectively, indicating good repeatability which is important from an application perspective. We also examined the response of the sensor to lower ethanol concentrations at a fixed applied voltage of 7 V (Figure 4c). Corresponding calibration curves (Figure 4d) clearly confirm that the sensor is able to detect ethanol gas. The responses to 1, 10, 20, 50, and 100 ppm ethanol were 3.3, 6.2, 8.1, 14.4 and 19.2, respectively. In addition, the response of the sensor in the presence of various levels of humid air with relative humidity (RH) levels of 0, 30, and 60% was studied at an applied voltage of 7 V. The response in dry air without humidity was 19.2, which decreased to 18.4 and 17.4 at 30 and 60% RH, respectively. Although the response decreased in the presence of humidity, it was still high enough for practical applications. In humid air, water molecules are adsorbed onto the sensor surface, resulting in a decrease in the number of adsorption sites. Thus, a smaller number of ethanol molecules are adsorbed on the sensor surface, and the response decreases [35].

 doi:10.20944/preprints202402.1218.v1

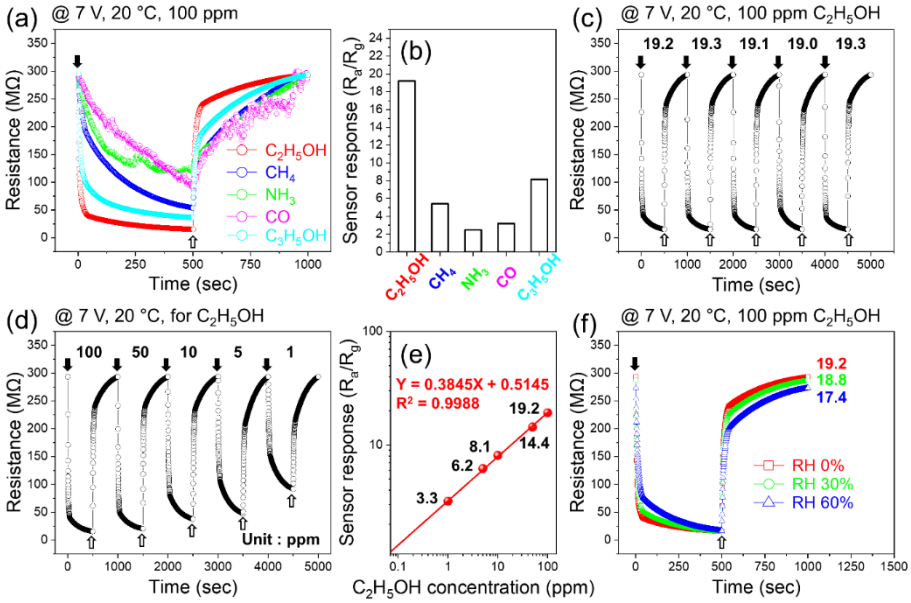

Figure 4. (**a**) Dynamic resistance curves of the sensor to 100 ppm various gases at 7 V applied voltage and (**b**) corresponding selectivity graph. (**c**) Repeatability of the sensor during five sequential cycles to 100 ppm ethanol at 7 V applied voltage. (**d**) Dynamic resistance curve and (**e**) corresponding calibration curve to low concentrations of ethanol at 7 V applied voltage. (**f**) Dynamic resistance curves to 100 ppm ethanol at 7 V applied voltage under 0, 30 and 60 % RH.

Next, we measured the sensing properties under flexible conditions. Digital photographs of the fabricated flexible gas sensors are presented in Figure 5a and b. In addition to flexibility, the sensor exhibits good transparency, which is important for some applications. Figure 5c and d display apparatus and conditions for bending and tilting the flexible sensors. The inset in Figure 5c shows an image of the sensor when bent.

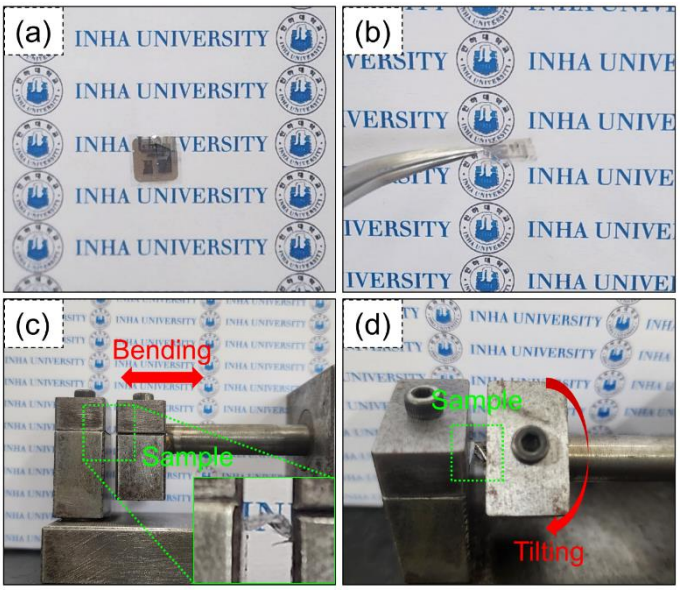

Figure 5. (**a**,**b**) Digital photographs of fabricated flexible gas sensor apparatus for (**c**) bending and (**d**) tilting of the flexible sensor. Inset in (**c**) shows higher magnification image.

The dynamic resistance curves of the flexible sensor to 10, 50, and 100 ppm of ethanol gas at an applied voltage of 7 V after various numbers of bending cycles (500, 1000, and 5000 cycles) are shown in Figure 6a. Figure 6b shows that the response did not change significantly in response to varying numbers of bending cycles. This demonstrated the high flexibility of the fabricated gas sensors. We

 doi:10.20944/preprints202402.1218.v1

also tested the sensing behavior after tilting the sensor 500, 1000, and 5000 times with various concentrations of ethanol at a fixed applied voltage of 7 V (Figure 6a). The response shows no significant changes in performance after these repeated tilting cycles, which again confirmed the high flexibility of the sensor.

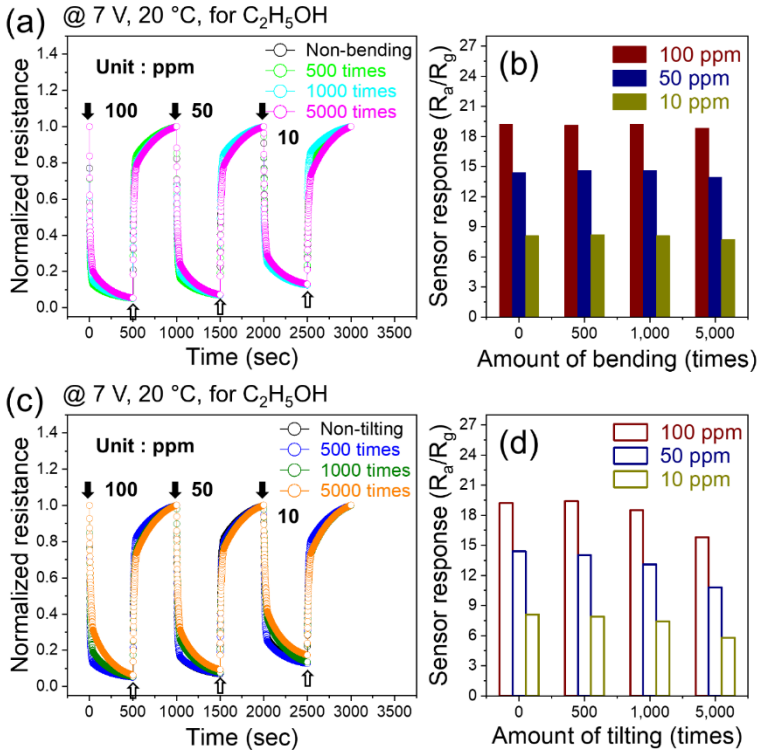

Figure 6. Dynamic resistance curves of flexible sensor to 10, 50 and 100 ppm ethanol gas at 7 V applied voltage after various (**a**) bending and (**c**) tilting cycles. Corresponding response versus (**b**) bending and (**d**) tilting cycles.

3.3. Gas Sensing Mechanism

The sensor in this study exhibited n-type sensing behavior, indicating that the sensing mechanism relies on the formation of an electron depletion layer (EDL) on the sensor surface, as is commonly accepted for n-type gas sensors. When the sensor is exposed to air, oxygen molecules with high electron affinity are adsorbed on the sensor surface, and electrons are extracted. The relevant reactions are as follows [36].

$$O_2(g) \rightarrow O_2(ads) \quad (1)$$

$$O_2(ads) + e^- \rightarrow O_2^-(ads), \text{T} \leq 150°\text{C} \quad (2)$$

$$O_2^-(ads) + e^- \rightarrow 2O^-, 150°\text{C} \leq \text{T} \leq 400°\text{C} \quad (3)$$

$$O^- + e^- \rightarrow O^{2-}, \text{T} > 400°\text{C} \quad (4)$$

Thus, an EDL was formed on the surface of the sensor, and the concentration of electrons in this layer was lower than that in the core. Upon exposure to ethanol, the following reaction is believed to occur at the sensing temperature [37].

$$C_2H_5OH + 7O^- \rightarrow 2CO_2 + 3H_2O + 7e^- \quad (5)$$

 doi:10.20944/preprints202402.1218.v1

Therefore, the reaction of the adsorbed oxygen species with the ethanol molecules leads electrons to be released onto the sensor surface. Thus, the thickness of the EDL and the resistance decreased. This results in the appearance of a sensing signal. Furthermore, in the contact area between the CFO grains, double Schottky barriers form in air, changing height upon exposure to ethanol, resulting in a change in resistance.

4. Conclusions

In brief, using PLD, a CFO thin film was deposited on a thin mica substrate using a solid CFO target to create a flexible ethanol sensor. AC-STEM confirmed that CFO was successfully deposited on the substrate with a well-defined interface. At 200 °C, the fabricated sensor exhibited the highest response of 19.2 to 100 ppm ethanol. To reduce the power consumption and sensing behavior, the sensor was operated in self-heating mode, where an applied voltage of 7 V resulted in a high sensor response of 19.2. The sensor was able to detect at little as 1 ppm of ethanol, and its response did not significantly decrease in humid air. The sensor also demonstrated high flexibility, and its performance did not degrade after bending and tilting up to 5000 times. Thus, this study realized the creation of a novel flexible, self-heating, selective, and sensitive ethanol sensor based on CFO on a mica substrate. The results presented in this manuscript pave the way for future studies in this area.

Author Contributions: Conceptualization, methodology, validation, formal analysis, investigation, data curation, writing—original draft preparation, J.H.K.; formal analysis, investigation, data curation, Y.U.C.; writing—original draft preparation, writing—review and editing, supervision, J.H.J.; conceptualization, methodology, validation, formal analysis, investigation, data curation, writing—original draft preparation, writing—review and editing, supervision, funding acquisition, J.-H.K. All authors have read and agreed to the published version of the manuscript.

Funding: This work was supported by INHA UNIVERSITY Research Grant.

Institutional Review Board Statement: Not applicable.

Informed Consent Statement: Not applicable.

Data Availability Statement: Data will be made available on request

Conflicts of Interest: The authors declare no conflicts of interest. The funders had no role in the design of the study; in the collection, analyses, or interpretation of data; in the writing of the manuscript; or in the decision to publish the results.

References

1. Jiang, B.; Zhou, T.; Zhang, L.; Han, W.; Yang, J.; Wang, C.; Sun, Y.; Liu, F.; Sun, P.; Lu, G. Construction of Mesoporous In_2O_3-ZnO Hierarchical Structure Gas Sensor for Ethanol Detection. *Sens. Actuators B* **2023**, *393*, 134203, doi:https://doi.org/10.1016/j.snb.2023.134203.
2. Feng, Y.; Chen, H.; Liu, Y.; Xu, B.; Jin, S.; Wang, Y. A Reusable Optical Fiber Sensor for Ethanol Gas Detection with a Large Concentration Range. *Opt. Fiber Technol.* **2023**, *80*, 103474, doi:https://doi.org/10.1016/j.yofte.2023.103474.
3. Shi, Y.; Li, X.; Sun, X.F.; Shao, X.; Wang, H.Y. Strategies for Improving the Sensing Performance of In_2O_3-Based Gas Sensors for Ethanol Detection. *J. Alloys Compd.* **2023**, *963*, 171190, doi:https://doi.org/10.1016/j.jallcom.2023.171190.
4. Phan, T.T.N.; Dinh, T.T.M.; Nguyen, M.D.; Dan Li; Phan, C.N.; Pham, T.K.; Nguyen, C.T.; Pham, T.H. Hierarchically Structured $LaFeO_3$ with Hollow Core and Porous Shell as Efficient Sensing Material for Ethanol Detection. *Sens. Actuators B* **2022**, *354*, 131195, doi:https://doi.org/10.1016/j.snb.2021.131195.
5. Mirzaei, A.; Janghorban, K.; Hashemi, B.; Bonyani, M.; Leonardi, S.G.; Neri, G. Highly Stable and Selective Ethanol Sensor Based on α-Fe_2O_3 Nanoparticles Prepared by Pechini Sol–Gel Method. *Ceram. Int.* **2016**, *42*, 6136–6144, doi:https://doi.org/10.1016/j.ceramint.2015.12.176.
6. Hussain, A.; Lakhan, M.N.; Soomro, I.A.; Ahmed, M.; Hanan, A.; Maitlo, A.A.; Zehra, I.; Liu, J.; Wang, J. Preparation of Reduced Graphene Oxide Decorated Two-Dimensional WSe_2 Nanosheet Sensor for Efficient Detection of Ethanol Gas. *Phys. E* **2023**, *147*, 115574, doi:https://doi.org/10.1016/j.physe.2022.115574.

7. Jiang, B.; Zhou, T.; Zhang, L.; Yang, J.; Han, W.; Sun, Y.; Liu, F.; Sun, P.; Zhang, H.; Lu, G. Separated Detection of Ethanol and Acetone Based on SnO_2-ZnO Gas Sensor with Improved Humidity Tolerance. *Sens. Actuators B* **2023**, *393*, 134257, doi:https://doi.org/10.1016/j.snb.2023.134257.
8. Wang, X.; Wang, X.; Wei, W.; Jiang, H.; Li, X.; Liu, G.; Zhu, Z.; Li, B.; Sheng, Y.; Zhou, J.; et al. Humidity-Resistant Ethanol Gas Sensors Based on Electrospun Tungsten-Doped Cerium Oxide Hollow Nanofibers. *Sens. Actuators B* **2023**, *393*, 134210, doi:https://doi.org/10.1016/j.snb.2023.134210.
9. Mojumder, S.; Das, T.; Das, S.; Chakraborty, N.; Saha, D.; Pal, M. Y and Al Co-Doped ZnO-Nanopowder Based Ultrasensitive Trace Ethanol Sensor: A Potential Breath Analyzer for Fatty Liver Disease and Drunken Driving Detection. *Sens. Actuators B* **2022**, *372*, 132611, doi:https://doi.org/10.1016/j.snb.2022.132611.
10. Arakawa, T.; Aota, T.; Iitani, K.; Toma, K.; Iwasaki, Y.; Mitsubayashi, K. Skin Ethanol Gas Measurement System with a Biochemical Gas Sensor and Gas Concentrator toward Monitoring of Blood Volatile Compounds. *Talanta* **2020**, *219*, 121187, doi:https://doi.org/10.1016/j.talanta.2020.121187.
11. Goel, N.; Kunal, K.; Kushwaha, A.; Kumar, M. Metal Oxide Semiconductors for Gas Sensing. *Eng. Rep.* **2023**, *5*, e12604, doi:https://doi.org/10.1002/eng2.12604.
12. Mirzaei, A.; Leonardi, S.G.; Neri, G. Detection of Hazardous Volatile Organic Compounds (VOCs) by Metal Oxide Nanostructures-Based Gas Sensors: A Review. *Ceram. Int.* **2016**, *42*, 15119–15141, doi:https://doi.org/10.1016/j.ceramint.2016.06.145.
13. Betty, C.A.; Choudhury, S.; Shah, A. Nanostructured Metal Oxide Semiconductors and Composites for Reliable Trace Gas Sensing at Room Temperature. *Surf. Interfaces* **2023**, *36*, 102560, doi:https://doi.org/10.1016/j.surfin.2022.102560.
14. Park, H.; K. J.-H.; Vivod, D.; Kim, S.; Mirzaei, A.; Zahn, D.; Park, C.; Kim, S.S.; Halik, M. Chemical-Recognition-Driven Selectivity of SnO_2-Nanowire-Based Gas Sensors. *Nano Today* **2021**, *40*, 101265, doi:https://doi.org/10.1016/j.nantod.2021.101265.
15. Katoch, G.; Himanshi; Jasrotia, R.; Prakash, J.; Verma, A.; Kandwal, A.; Godara, S.K.; Verma, R.; Raja, V.; Kumar, G. Crystal Structure, Synthesis, Properties and Potential Applications of Cobalt Spinel Ferrite: A Brief Review. *Mater. Today: Proc.* **2023**, doi:https://doi.org/10.1016/j.matpr.2023.03.585.
16. Ahmad, S.I. Nano Cobalt Ferrites: Doping, Structural, Low-Temperature, and Room Temperature Magnetic and Dielectric Properties – A Comprehensive Review. *J. Magn. Magn. Mater.* **2022**, *562*, 169840, doi:https://doi.org/10.1016/j.jmmm.2022.169840.
17. Prasad, P.D.; Hemalatha, J. Enhanced Magnetic Properties of Highly Crystalline Cobalt Ferrite Fibers and Their Application as Gas Sensors. *J. Magn. Magn. Mater.* **2019**, *484*, 225–233, doi:https://doi.org/10.1016/j.jmmm.2019.04.026.
18. Joshi, S.; Kamble, V.B.; Kumar, M.; Umarji, A.M.; Srivastava, G. Nickel Substitution Induced Effects on Gas Sensing Properties of Cobalt Ferrite Nanoparticles. *J. Alloys Compd.* **2016**, *654*, 460–466, doi:https://doi.org/10.1016/j.jallcom.2015.09.119.
19. Wei, K.; Huai, H.-X.; Zhao, B.; Zheng, J.; Gao, G.-Q.; Zheng, X.-Y.; Wang, C.-C. Facile Synthesis of $CoFe_2O_4$ Nanoparticles and Their Gas Sensing Properties. *Sens. Actuators B* **2022**, *369*, 132279, doi:https://doi.org/10.1016/j.snb.2022.132279.
20. Le, D.T.T.; Long, N.D.H.; Xuan, C.T.; Toan, N.V.; Hung, C.M.; Duy, N.V.; Theu, L.T.; Dinh, V.A.; Hoa, N.D. Porous $CoFe_2O_4$ Nanorods: VOC Gas-Sensing Characteristics and DFT Calculation. *Sens. Actuators B* **2023**, *379*, 133286, doi:https://doi.org/10.1016/j.snb.2023.133286.
21. Rathore, D.; Kurchania, R.; Pandey, R.K. Gas Sensing Properties of Size Varying $CoFe_2O_4$ Nanoparticles. *IEEE Sensors J.* **2015**, *15*, 4961–4966, doi:10.1109/JSEN.2015.2432035.
22. Xiangfeng, C.; Dongli, J.; Yu, G.; Chenmou, Z. Ethanol Gas Sensor Based on $CoFe_2O_4$ Nano-Crystallines Prepared by Hydrothermal Method. *Sens. Actuators B* **2006**, *120*, 177–181, doi:https://doi.org/10.1016/j.snb.2006.02.008.
23. Yun, J.; Cho, M.; Lee, K.; Kang, M.; Park, I. A Review of Nanostructure-Based Gas Sensors in a Power Consumption Perspective. *Sens. Actuators B* **2022**, *372*, 132612, doi:https://doi.org/10.1016/j.snb.2022.132612.
24. Fàbrega, C.; Casals, O.; Hernández-Ramírez, F.; Prades, J.D. A Review on Efficient Self-Heating in Nanowire Sensors: Prospects for Very-Low Power Devices. *Sens. Actuators B* **2018**, *256*, 797–811, doi:https://doi.org/10.1016/j.snb.2017.10.003.
25. Alrammouz, R.; Podlecki, J.; Abboud, P.; Sorli, B.; Habchi, R. A Review on Flexible Gas Sensors: From Materials to Devices. *Sens. Actuators A* **2018**, *284*, 209–231, doi:https://doi.org/10.1016/j.sna.2018.10.036.
26. Bag, A.; Lee, N.-E. Recent Advancements in Development of Wearable Gas Sensors. *Adv. Mater. Technol.* **2021**, *6*, 2000883, doi:https://doi.org/10.1002/admt.202000883.
27. Liu, J.; Feng, Y.; Tang, R.; Zhao, R.; Gao, J.; Shi, D.; Yang, H. Mechanically Tunable Magnetic Properties of Flexible $SrRuO_3$ Epitaxial Thin Films on Mica Substrates. *Adv. Electron. Mater.* **2018**, *4*, 1700522, doi:https://doi.org/10.1002/aelm.201700522.
28. Hyeon, D.Y.; Park, K.-I. Piezoelectric Flexible Energy Harvester Based on $BaTiO_3$ Thin Film Enabled by Exfoliating the Mica Substrate. *Energy Technol.* **2019**, *7*, 1900638, doi:https://doi.org/10.1002/ente.201900638.

29. Haider, A.J.; Alawsi, T.; Haider, M.J.; Taha, B.A.; Marhoon, H.A. A Comprehensive Review on Pulsed Laser Deposition Technique to Effective Nanostructure Production: Trends and Challenges. *Opt. Quantum Electron.* **2022**, *54*, 488, doi:10.1007/s11082-022-03786-6.
30. Oh, K.L.; Kwak, Y.M.; Kong, D.S.; Ryu, S.; Kim, H.; Jeen, H.; Choi, S.; Jung, J.H. Mechanical Stability of Ferrimagnetic $CoFe_2O_4$ Flexible Thin Films. *Curr. Appl. Phys.* **2021**, *31*, 87–92, doi:10.1016/j.cap.2021.08.004.
31. Barlow, S.G. and Manning, D.A.C., Influence of Time and Temperature on Reactions and Transformations of Muscovite Mica. *Br. Ceram. Trans.* **1999**, *98*, 122–126.
32. Koma, A. Van Der Waals Epitaxy—a New Epitaxial Growth Method for a Highly Lattice-Mismatched System. *Thin Solid Films* **1992**, *216*, 72–76, doi:https://doi.org/10.1016/0040-6090(92)90872-9.
33. Ueno, K.; Saiki, K.; Shimada, T.; Koma, A. Epitaxial Growth of Transition Metal Dichalcogenides on Cleaved Faces of Mica. *J. Vac. Sci. Technol., A* **1990**, *8*, 68–72, doi:10.1116/1.576983.
34. Zheng, K.; Yuan, Y.; Zhao, L.; Chen, Y.; Zhang, F.; Song, J.; Qu, J. Ultra-Compact, Low-Loss Terahertz Waveguide Based on Graphene Plasmonic Technology. *2D Mater.* **2019**, *7*, 015016, doi:10.1088/2053-1583/ab5546.
35. Kim, J.-H.; Mirzaei, A.; Sakaguchi, I.; Hishita, S.; Ohsawa, T.; Suzuki, T.T.; Kim, S.S.; Saito, N. Decoration of Pt/Pd Bimetallic Nanoparticles on Ru-Implanted WS_2 Nanosheets for Acetone Sensing Studies. *Appl. Surf. Sci.* **2023**, *641*, 158478, doi:https://doi.org/10.1016/j.apsusc.2023.158478.
36. Zheng, Z.; Liu, K.; Zhou, Y.; Zhang, Z.; Su, H.; Nie, X.; Debliquy, M.; Yu, Z.; Zhang, C. Spinel Type MCo_2O_4 (M = Mn, Mg, Ni, Cu, Fe and Zn) for Chemoresistance Gas Sensors. *Mater. Today Chem.* **2024**, *36*, 101928, doi:https://doi.org/10.1016/j.mtchem.2024.101928.
37. Cheng, Y.; Shao, T.; Dong, J.; Kou, H.; Zhang, F.; Guo, J.; Liu, X. MOF-Derived SnO_2@ZnO Ethanol Sensors with Enhanced Gas Sensing Properties. *Vacuum* **2023**, *216*, 112440, doi:https://doi.org/10.1016/j.vacuum.2023.112440.